Automated Detection and Analysis of Resident Space Objects with the 1.3-meter Eugene Stansbery-Meter Class Autonomous Telescope

Paul Hickson[(1)], Brent Buckalew[(2)], and Corbin Cruz[(2)]

[(1)] University of British Columbia, Department of Physics and Astronomy, 6224 Agricultural Road, Vancouver, BC, V6T 1Z1, Canada, hickson@physics.ubc.ca
[(2)] Jacobs, NASA Johnson Space Center, Mail Code XI5-9E, 2101 NASA Parkway, Houston, TX 77058, USA; brent.a.buckalew@nasa.gov; corbin.l.cruz@nasa.gov

Abstract

Optical telescopes dedicated to the detection of orbital debris employ large-area detectors that generate a large number of images each night. Such surveys require automated data analysis pipelines that process the images and detect moving objects. We present an overview of the data analysis pipeline employed by the 1.3-meter Eugene Stansbery Meter-Class Autonomous Telescope (ES-MCAT) on Ascension Island, operated by NASA's Orbital Debris Program Office. The pipeline enfolds the astrometric and photometric calibration of the images, star-trail removal, object detection, correlation over multiple, sequential image frames, and orbital parameter estimation. The performance of the pipeline was investigated by means of Monte-Carlo simulations in which simulated object tracks were inserted into ES-MCAT images and then processed by the pipeline. This technique allows one to confidently estimate the completeness for the detection of resident space objects as a function of apparent magnitude and angular velocity. This paper discusses these techniques and provides examples using actual data.

1 Introduction

The Eugene Stansbery Meter-Class Autonomous Telescope (ES-MCAT) is a 1.3-metre aperture optical telescope located on Ascension Island [1–5]. A joint project of NASA and the US Air Force Research Laboratory, the telescope is dedicated to space debris research. It is designed to statistically sample resident space objects (RSOs), which include satellites, rocket bodies, and orbital debris at all altitudes. The primary mission of ES-MCAT is to characterize the orbital-debris environment in or near geosynchronous orbit (GEO).

The telescope has wide-field optics and is equipped with a 4096×4096-pixel CCD camera that covers a 41×41 arcmin field of view. One can select from a suite of Sloan and Johnson optical filters. The facility operates autonomously, typically acquiring on the order of 1000 images per night. The data are autonomously processed the following day to detect and characterize moving objects. The operations and the data processing are performed by customized Observatory Control System (OCS) software developed by Euclid Research Corp. [6].

The most common operational mode for ES-MCAT is to acquire a series of seven sequential images of the same field, while tracking at a constant rate (which may be zero in the case of observations of objects in GEO). The images are filled with star trails, which are different for each image, but objects of interest are typically point-like or elongated, and generally appear in more than one image. They can be identified by comparing their positions in the image sequence, as they move at nearly constant angular rates.

In order to assess the performance of both the telescope and the OCS data-processing algorithms, Monte-Carlo simulations were performed. Simulated images of stationary and moving objects were added to ES-MCAT images in these simulations, which were then processed by the pipeline. By comparing the objects that were detected with those that were simulated, the completeness, false alarm rate, and photometric accuracy was determined as a function of object magnitude and angular rate. This paper describes the data-processing pipeline, the Monte-Carlo simulations, and presents our results.

2 Object Detection Pipeline

Some details of the image processing steps and algorithms used by OCS are described in [5] and [6]. Since then, some of the data analysis steps have been further refined. Here are provided a summary and update. Images are first preprocessed by subtracting a median dark image and dividing by a median flat-field image generated from observations of the sky during twilight. Cosmic rays are removed by two-dimensional median filtering. A two-dimensional high-pass spatial filter is then applied to remove variations in the background, caused primarily by clouds.

Each preprocessed image is calibrated by comparing stars in the image with those in the *Gaia* DR3 catalog [7, 8]. OCS creates a simulated image of the field in which *Gaia* stars are inserted using the positions and fluxes derived from the catalog. *Gaia* G, G_{BP}, and G_{RP} magnitudes are transformed to the Sloan band of the observations using the relations provided in the *Gaia* DR3 documentation. Stars in the simulated image have a Racine intensity profile [9] having the same full width at half maximum intensity (FWHM) as the stars in the image. This profile uses the sum of two Moffat functions to accurately reproduce both the core of the point spread function and the halo. Pixel coordinates of the simulated *Gaia* stars are determined using approximate world coordinate system (WCS) parameters based on the telescope position reported by the telescope control system (TCS), and the known camera orientation and image scale.

An iterative cross-correlation analysis is then performed, between the simulated and measured star images. This provides position offsets, and any small corrections to the image scale and rotation. These are used to update the WCS fields in the FITS header.

The analysis also provides the photometric zero point for the image (the difference between true magnitude and instrumental magnitude) and estimates of the astrometric and photometric uncertainties. For sidereal-tracked images, the typical astrometric accuracy is ~ 1 arcsec and the photometric accuracy is ~ 0.1 magnitude, which includes the uncertainties in transformation between the *Gaia* and Sloan bands. For non-sidereal images, the calibration is performed using the star trails in the image. Simulated star trails are created using the hour angle and declination tracking rates reported by the TCS.

Calibrated images are then analyzed to detect all objects in the image. The default algorithm presently used by OCS is corrected isophotal photometry. In standard isophotal photometry, objects are defined by connected pixels that have intensities above a specified threshold, typically a few times the root mean square (RMS) noise in the image, after background subtraction. The object flux is taken to be the sum of the intensities of the pixels in the object. This works well for bright objects but is systematically biased for faint objects. The reason is that much of the object flux is contained in pixels that have intensity below the threshold and are therefore not counted, resulting in the flux being underestimated. To remove this bias, OCS applies an empirical correction to the flux that depends both on the ratio of the maximum intensity in the object to the threshold and on the axis ratio of the object, which is unity for circular images but can be large for trailed images. The output, for each image, is a list of objects containing positions, magnitudes, and other photometric parameters. In the case of non-sidereal tracking, star trails are masked before object detection. The mask is created based on the known positions of *Gaia* stars, the telescope tracking rates, the exposure time, and the measured FWHM for the image.

The most common operational mode for ES-MCAT is to acquire a series of seven sequential images of the same field, while tracking at a constant rate, which may be zero arcsec/s in hour angle and declination in the case of GEO observations. The images are filled with star trails, which are different for each image, but objects of interest are typically point-like and move little from one image to the next. The next step in the processing pipeline is to examine the photometry files for each sequence of images and identify objects that are stationary or moving through the images at a constant angular rate. OCS produces an object file that lists all such objects found by its matching algorithm in the image sequences. For an object to be included, it must be detected in at least four images of the sequence. OCS then attempts to derive orbital elements for each object and rejects those for which a satisfactory orbital fit cannot be found. In this way, accidental alignments of star-trail residuals, and other artifacts, are eliminated.

3 Simulations

Two types of studies were performed. In the first, the detection completeness and photometric accuracy of the OCS object detection and photometric algorithms were estimated by adding simulated objects to individual images. For each image, the OCS object detection program was then applied, and a comparison made between simulated and measured objects.

The second study examined the detection efficiency of the OCS matching algorithm for the detection of moving objects appearing in a sequence of images. Simulated objects were given random angular velocities and directions and added to the images. The position of each object in each image was calculated based on the angular rates and the relative observation times of the images. The sequence of images was then processed by the OCS pipeline. The resulting object files were compared with the positions and magnitudes of the simulated objects to find the detection probability (completeness) as a function of the magnitude and angular rate of the simulated objects.

3.1 Image data

Two sequences of images were employed for these studies. Both were obtained by ES-MCAT on the night of 22 June 2020. The file names, and relevant metadata, are listed in Table 1. The column headings are image file name, right ascension, declination, galactic latitude, magnitude zero-point, mean FWHM along the minor axes of star or star trail images in arcsec, and tracking mode.

Table 1. Parameters of images used for the analysis.
All have an exposure time of 10 s and used the r' filter.

File	RA	DEC	Gal Lat	Zero pt	FWHM	Mode
2020174-00036_p.fits	13:25:39.5	-08:49:18	53.106	24.084	2.419	st
2020174-00037_p.fits	13:25:39.5	-08:49:18	53.106	24.073	2.246	st
2020174-00038_p.fits	13:25:39.5	-08:49:18	53.106	24.076	2.392	st
2020174-00039_p.fits	13:25:39.5	-08:49:18	53.106	24.005	2.162	st
2020174-00040_p.fits	13:25:39.6	-08:49:18	53.106	24.016	2.176	st
2020174-00055_p.fits	13:25:39.5	-08:49:16	53.106	24.058	2.331	st
2020174-00056_p.fits	13:25:39.5	-08:49:18	53.106	24.036	2.240	st
2020174-00175_p.fits	17:08:12.0	-17:30:00	13.440	24.720	3.033	rt
2020174-00176_p.fits	17:08:51.2	-17:30:02	13.312	24.496	2.795	rt
2020174-00177_p.fits	17:09:29.7	-17:30:03	13.185	24.524	2.811	rt
2020174-00178_p.fits	17:10:08.3	-17:30:03	13.059	24.191	2.756	rt
2020174-00179_p.fits	17:10:47.2	-17:30:05	12.931	24.085	3.277	rt
2020174-00180_p.fits	17:11:26.4	-17:30:05	12.802	24.181	3.300	rt
2020174-00181_p.fits	17:12:05.9	-17:30:07	12.672	24.118	3.310	rt

The first sequence of seven images was acquired using st (sidereal track) mode, in which the telescope tracks at the sidereal rate. Accordingly, the star images are circular. The Sloan r' filter was used and the exposure time was 10 s for all images. For this sequence, the galactic latitude was 53°, so the density of star images is relatively low. The second sequence was acquired using rt (rate track) mode. In this case, the hour-angle and declination tracking rates were set equal to zero (*i.e.,* the telescope was stationary), to facilitate the detection of objects in GEO. The exposure time for all images was 10 seconds and the image scale was 0.60 arcsec/pixel. Accordingly, the star images were trailed by typically 150 arcsec (250 pixels). The r' filter was used for all images. For this sequence, the galactic latitude was just 13°, and the density of star trails was quite high.

3.2 Detection limits and photometric accuracy for individual images

For this analysis both st-mode and rt-mode images were employed. For all simulations, images of objects were generated by convolving a linear track (or a point for untrailed objects) with a Racine function having the same FWHM as the star images.

In the first set of simulations, 100 simulated objects were added to each st-mode image at random positions and having magnitudes randomly selected from a uniform probability distribution in the range [12, 20.99]. As there are 7 files in the sequence, this resulted in a total of 700 simulated objects being created and processed. The images were then analyzed by the OCS object detection program. Positions and magnitudes of the detected objects were then compared with those of the simulated objects.

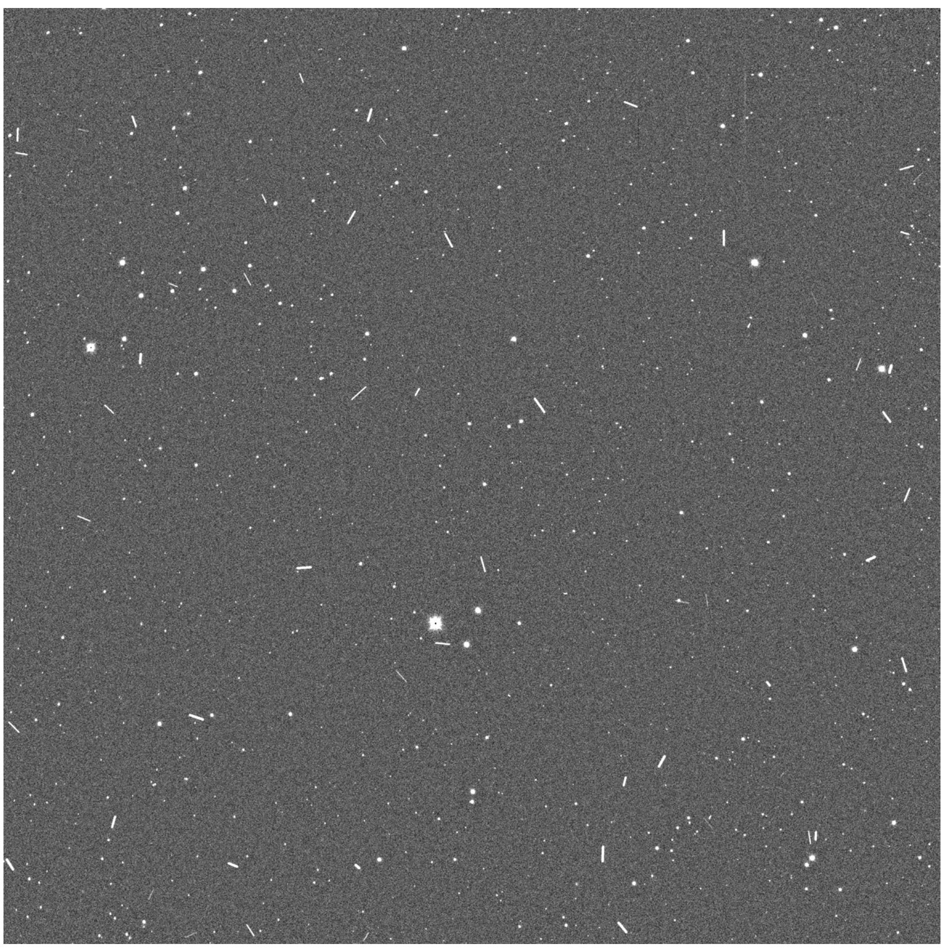

Fig. 1. Frame 40 of the st-mode sequence, with 100 simulated objects added. The objects are assigned random angular rates in the RA and Dec directions, each drawn from a uniform probability distribution in the range [-4.0, 4.0] arcsec/s.

This process was then repeated for objects moving at random angular rates up to a maximum of 2 arcsec/s in the RA and Dec directions, corresponding to a maximum possible angular rate of 2.83 arcsec/s along the track. Finally, this was repeated once more, but with the maximum angular rate set to 4 arcsec/s in each of the RA and Dec directions, corresponding to a maximum possible angular rate of 5.66 arcsec/s along the track. An example of one of these last simulations in Fig. 1 shows the original star field with the simulated trailed objects added.

For the second set of simulations, rt-mode images were used. The procedure was the same as for the st-mode images, except in this case star trails were masked before object detection. This is the default procedure used by the OCS pipeline when searching for objects in non-sidereal images.

3.3 Detection of moving objects in sequences of images

This analysis involved only rt-mode images. Again, three sets of simulations were obtained, corresponding to maximum RA and Dec angular rates of 0, 2, and 4 arcsec/s, corresponding to maximum rates along the track of 3.83 and 5.66 arcsec/s, respectively. For each set, random positions, magnitudes in the range [12, 20.99], and angular rates were generated for 100 simulated objects. Images of these objects were then added to all images in the sequence.

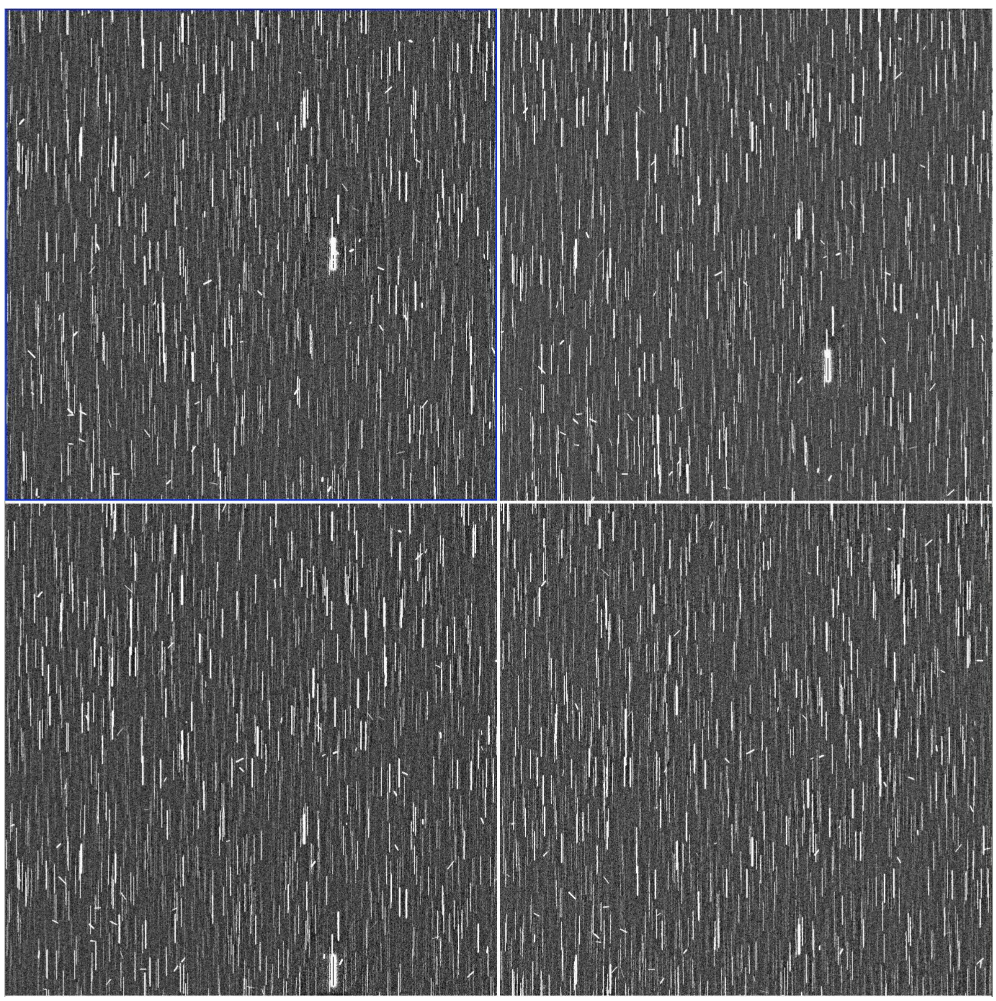

Fig. 2. Frames 175-178 of the rt-mode sequence, with 100 simulated objects added. The objects have different positions in each frame, consistent with their assigned angular rates. The maximum angular rate is 5.66 arcsec/s.

For the central image of the sequence (*i.e.*, the fourth file in the sequence), the objects were placed at their assigned positions. Positions of the objects in the other files were determined by propagating the positions according to their angular rates and the relative times of their exposure midpoints. The images were then processed by the relevant section of the OCS pipeline to detect moving (or stationary) objects in the sequence. This process was repeated 10 times, to increase the statistical accuracy. In total, 1000 simulated objects were processed.

As an example, Fig. 2 shows the first four frames of the rt-mode sequence with the simulated trailed objects added. The maximum angular rate for the objects is 5.66 arcsec/s and the simulated objects have moved between the two frames, as they should.

4 Results

Magnitude limits for 50% completeness for all simulations are presented in Table 2. The first section of the table shows detection limits for simulated objects inserted into individual sidereal-tracked images. The second section of the table shows detection limits for simulated objects inserted into individual non-sidereal images, some of which are shown in Fig. 2. The third section shows detection limits for objects inserted in a sequence of non-sidereal images and recovered by the OCS pipeline.

Table 2. Magnitude Limits for 50% Completeness

Mode	Simulation	Max. rate (arcsec/s)	Mag. limit (r')
st	individual	0	20.2
st	individual	2.83	19.0
st	individual	5.66	18.3
rt	individual	0	17.7
rt	individual	2.83	16.8
rt	individual	5.66	15.1
rt	sequence	0	17.8
rt	sequence	2.83	16.3
rt	sequence	5.66	15.1

4.1 Detection limits for individual images

For the single-image simulations, the completeness is plotted as a function of magnitude in Figs. 3 and 4.

4.2 Detection of moving objects in sequences of images

Detection limits for 50% completeness for the sequence simulations are given in the third section of Table 2. The completeness is plotted as a function of magnitude in Fig. 5.

4.3 Photometric accuracy

Photometric accuracy was estimated for simulated objects placed in calibrated ES-MCAT images by comparing the magnitudes measured by OCS with the magnitudes used to generate the simulated objects. An example is shown in Fig. 6, in which the magnitude error is plotted vs. the magnitude used to generate the simulated image (*i.e.*, true magnitude).

It is important to note that the errors shown here reflect only the accuracy of the object detection and measurement process. They do not include uncertainties in the photometric transformations between the *Gaia* bands and the Sloan bands used by ES-MCAT. Those are typically on the order of 0.07 to 0.10 magnitudes.

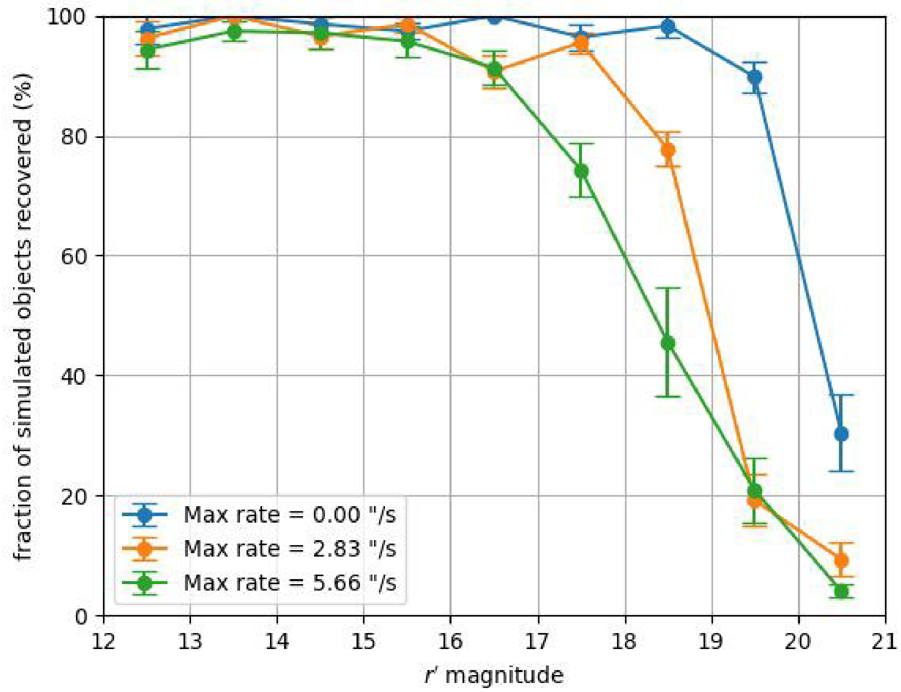

Fig. 3. Completeness for a st-mode image at high galactic latitude. The percent of simulated objects recovered is plotted vs. magnitude. Error bars indicate 1σ uncertainties.

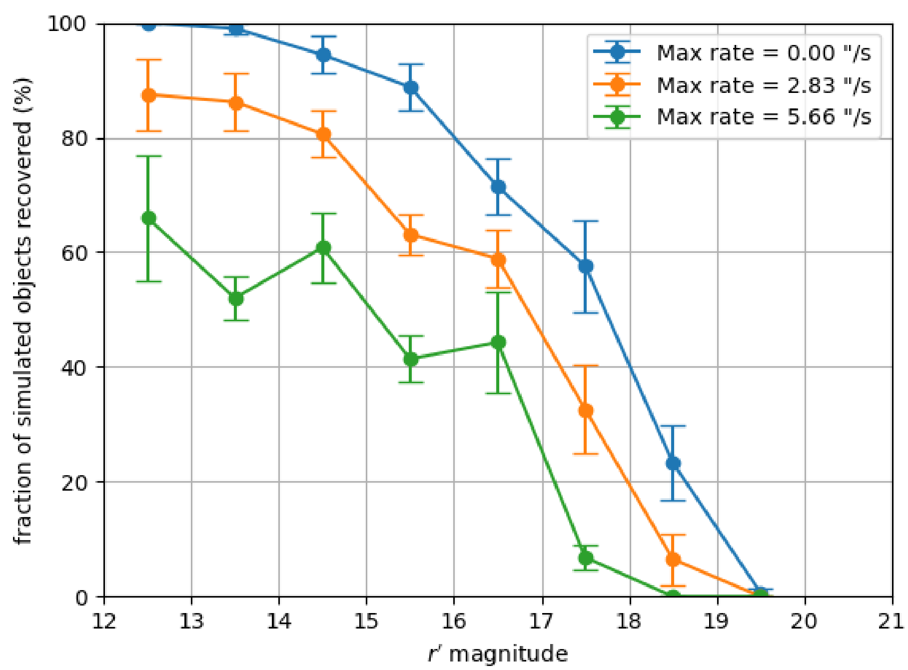

Fig. 4. Completeness for an rt-mode untracked image (*i.e.*, GEO observations) at low galactic latitude. The percent of simulated objects recovered is plotted vs. magnitude. Error bars indicate 1σ uncertainties.

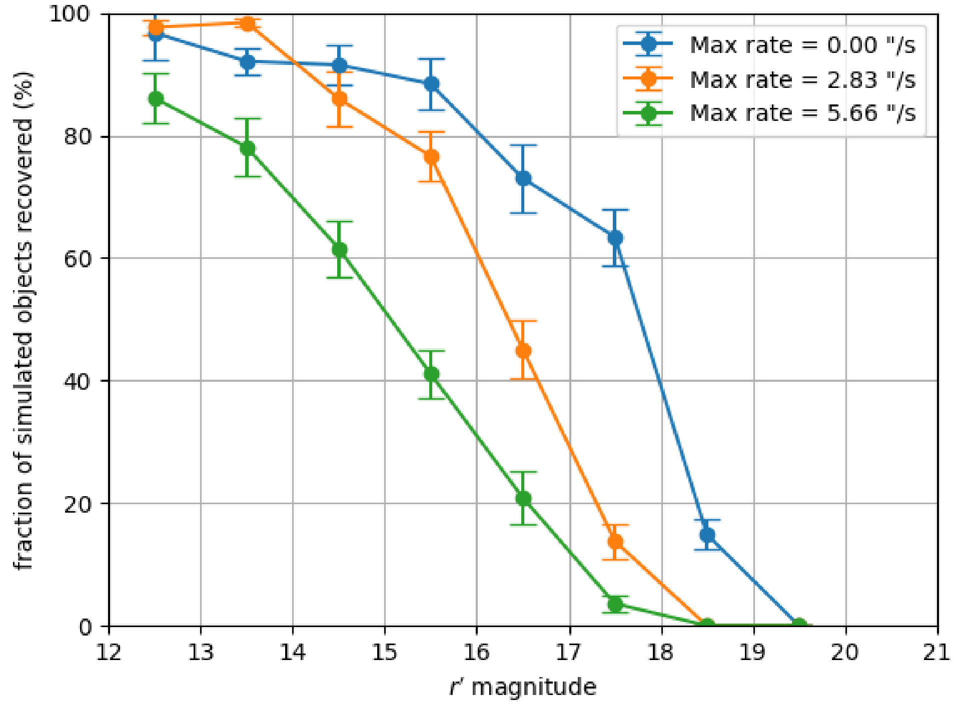

Fig. 5. Completeness for objects moving through a sequence of untracked images at low galactic latitude. The percent of simulated objects recovered in four or more images is plotted vs. magnitude. Error bars indicate 1σ uncertainties.

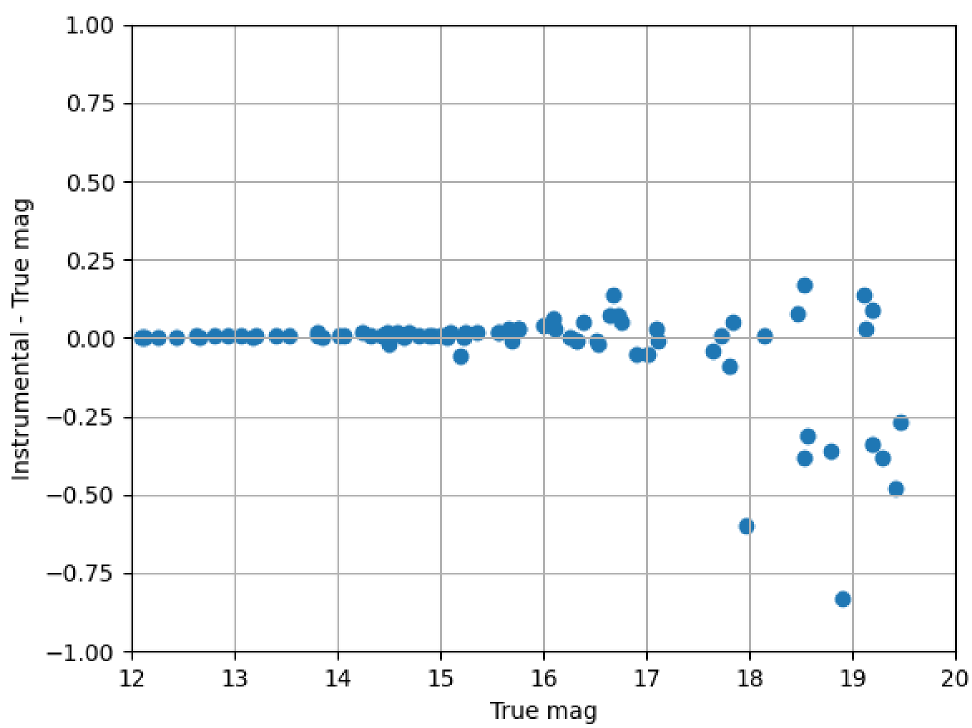

Fig. 6. Magnitude residuals vs. true magnitude for stationary objects placed in st-mode images.

5 Discussion

The simulations show that for star-like objects (*i.e.,* untrailed) inserted in sidereal-tracked images, the 50% completeness limit, for a signal-to-noise ratio of 5.0, is r' = 20.2. The completeness exceeds 90% even to r' = 19.5. For trailed objects inserted in st-mode images, the limiting magnitude is brighter, as is expected. The 50% completeness limits are r' = 19.0 and 18.3 for maximum angular rates of 2.83 and 5.66 arcsec/s, respectively. There are several factors that enter here. For a given magnitude, trailed images have lower surface brightness, and more often fall below the threshold intensity for detection. Also, their images cover more pixels, resulting in greater background noise inevitably contaminating the image and reducing the signal-to-noise ratio. Finally, trailed images are more likely to blend with brighter star images, resulting in the object being missed (its flux is just added to that of the star). These effects are unavoidable.

The second section of Table 2 gives 50% detection limits for objects inserted in rt-mode images. These limits are two to three magnitudes brighter than the corresponding limits for st-mode images. There are several reasons for this. The rt-mode images that were studied are all at low galactic latitude and as a result, there are many star trails contaminating the images. This results in more objects being missed and, for trailed objects, there is a greater chance of the flux being underestimated as a portion of the trail might overlap a star trail and be masked.

The completeness limits for the detection of moving objects in a sequence of images are listed in the third section of Table 2. These values are statistically the same as those for the detection of objects in individual rt-mode images. This indicates that the algorithm used by OCS is effective at finding most detectable objects.

Figure 6 shows typical magnitude residuals for untrailed images. The photometric accuracy is typically better than 0.05 magnitudes for objects brighter than r' = 17, with a typical RMS error of about 0.01 magnitude. For r' > 17.0, the scatter in the points increases to an RMS of about 0.2 magnitude at r' = 20. There is no evident systematic bias in the magnitudes. For trailed objects, the photometric accuracy is also very good, but only for r' < 16.0, about a magnitude brighter limit than for untrailed objects.

6 Summary and Conclusions

This study has examined the performance of the ES-MCAT telescope, and the OCS data analysis pipeline, by means of Monte-Carlo simulations using images obtained with both sidereal and non-sidereal tracking rates. The object detection completeness vs. magnitude was determined for both st and rt observing modes, for trailed as well as untrailed objects. Magnitude limits for 50% completeness range from r' = 20.2 for untrailed objects in st-mode images at high galactic latitude to r' = 15.1 for objects having angular rates of up to 5.66 arcsec/s inserted in rt-mode images acquired at low galactic latitude. These are typical best-case and worst-case scenarios.

For untrailed objects inserted in st-mode images at high galactic latitude, magnitude errors are less than 0.05 for r' < 17.0, with a typical RMS error of about 0.01 magnitude. There is no evident systematic error in the magnitudes. The magnitude errors are also very small for trailed objects, but only to r' ~ 16.

For the detection of moving objects in sequences of images, the detection limits are nearly identical to those of individual rt-mode images, indicating OCS is very efficiently finding the objects.

Completeness studies such as this can be used to correct the results obtained by optical sensors. All sensors have limitations, as do the algorithms used to derived object counts. Once the completeness has been determined, as a function of parameters such as magnitude and angular rate, the counts can be corrected statistically for objects that were missed. This completeness could be used to improve the accuracy and reliability of the results.

7 Acknowledgements

This work was funded under contract with NASA. It has made use of data from the European Space Agency (ESA) mission *Gaia* (https://www.cosmos.esa.int/gaia), processed by the *Gaia* Data Processing and Analysis Consortium (DPAC, https://www.cosmos.esa.int/web/gaia/dpac/consortium). Funding for the DPAC has been provided by national institutions, in particular the institutions participating in the *Gaia* Multilateral Agreement.

8 References

1. S. Lederer, E. G. Stansbery, H. M. Cowardin, P. Kervin, and P. Hickson. The NASA Meter Class Autonomous Telescope: Ascension Island. In S. Ryan, editor, *Proceedings of the Advanced Maui Optical and Space Surveillance Technologies Conference*, id. E82, 2013.
2. S. Lederer, J. Frith, L. F. Pace, *et al*. NASA's Newest Orbital Debris Ground-based Telescope Assets: MCAT and UKIRT. In S. Ryan, editor, *Proceedings of the Advanced Maui Optical and Space Surveillance Technologies Conference*, id. E79, 2014.
3. S. Lederer, Pace. L., P. Hickson, *et al*. Deploying the NASA Meter Class Autonomous Telescope (MCAT) on Ascension Island. In S. Ryan, editor, *Proceedings of the Advanced Maui Optical and Space Surveillance Technologies Conference*, id. 34, 2015.
4. S. M. Lederer, P. Hickson, H. M. Cowardin, *et al*. NASA's Optical Program on Ascension Island: Bringing MCAT to Life as the Eugene Stansbery-Meter Class Autonomous Telescope (ES-MCAT). In S. Ryan, editor, *Proceedings of the Advanced Maui Optical and Space Surveillance Technologies Conference*, id. 105, 2017.
5. S. Lederer, P. Hickson, and B. Buckalew. NASA's Orbital Debris JAO/ES-MCAT Optical Telescope Facility on Ascension Island. In *First International Orbital Debris Conference*, volume 2109 of *LPI Contributions*, page 6039, December 2019.
6. P. Hickson. OCS: A flexible observatory control system for robotic telescopes with application to detection and characterization of orbital debris. In *First International Orbital Debris Conference*, volume 2109 of *LPI Contributions*, page 6066, December 2019.
7. Gaia Collaboration, T. Prusti, J. H. J. de Bruijne, *et al*. The Gaia mission. *Astronomy and Astrophysics*, 595, pp. A1, 2016.
8. Gaia Collaboration, A. Vallenari, A. G. A. Brown, *et al*. Gaia Data Release 3. Summary of the content and survey properties. *Astronomy and Astrophysics*, 674, pp. A1, 2023.
9. R. Racine. The telescopic point-spread function. *Publications of the Astronomical Society of the Pacific*, 108, pp. 699–705, 1996.